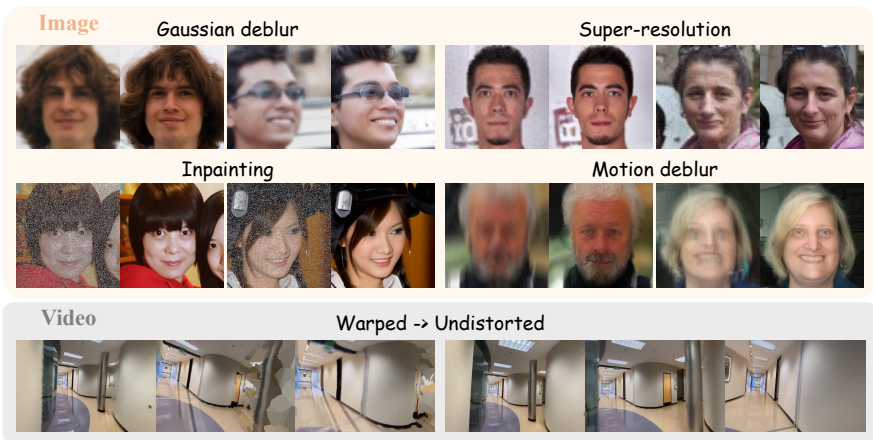


# Coarse-Guided Visual Generation via Weighted $h$ -Transform Sampling

Yanghao Wang\*, Ziqi Jiang\*, Zhen Wang, and Long Chen†

The Hong Kong University of Science and Technology  
 ywangtg@connect.ust.hk, zhenwang@ust.hk, longchen@ust.hk  
<https://github.com/HKUST-LongGroup/Coarse-guided-Gen>



**Fig. 1:** Given a coarse visual sample (left one in each pair) as the guidance, our method generates its corresponding refined result (right one) in a training-free manner.

**Abstract.** Coarse-guided visual generation, which synthesizes fine visual samples from degraded or low-fidelity coarse references, is essential for various real-world applications. While training-based approaches are effective, they are inherently limited by high training costs and restricted generalization due to paired data collection. Accordingly, recent training-free works propose to leverage pretrained diffusion models and incorporate guidance during the sampling process. However, these training-free methods either require knowing the forward (fine-to-coarse) transformation operator, *e.g.*, bicubic downsampling, or are difficult to balance between guidance and synthetic quality. To address these challenges, we propose a novel guided method by using the  $h$ -transform, a tool that can constrain stochastic processes (*e.g.*, sampling process) under desired conditions. Specifically, we modify the transition probability at each sampling timestep by adding to the original differential equation with a drift function  $h$ , which approximately steers the generation toward the ideal fine sample. To address unavoidable approximation errors, we introduce

a noise-level-aware schedule that gradually de-weights the  $h$  term as the error increases, ensuring both guidance adherence and high-quality synthesis. Extensive experiments across diverse image and video generation tasks demonstrate the effectiveness and generalization of our method.

**Keywords:** Guided Visual Generation · Diffusion Model · Doob’s  $h$ -Transform

## 1 Introduction

Recent advances in diffusion [14, 44] and flow matching [27, 28] models have demonstrated remarkable visual generation capability. Benefited from large-scale pretraining, high-quality samples can be generated by existing unconditional and text-to-visual (T2V) models [23, 39, 49] in the case of without guidance or only with text guidance. However, some real-world applications (*e.g.*, deblurring and super-resolution) always require a coarse visual sample to guide synthesis, which these pretrained unconditional and T2V models cannot handle directly. Thus, recent works [5–7, 19, 21, 31, 41, 44] aim to solve such a **coarse-guided visual generation** task (*cf.*, Figure 1): given a *coarse visual sample* (*e.g.*, a blurred image, or a warped video) as the guidance, the model needs to generate the *corresponding refined sample* (*e.g.*, a clear image, or an undistorted video).

A straightforward approach to coarse-guided visual generation is to train translation networks. As shown in Figure 2(a), previous studies [8, 56, 59] try to train from scratch or finetune a translation model with paired coarse-fine data. For different types of coarse sample (*e.g.*, low-resolution images, blurred images, and warped videos), additional/existing models must be trained/finetuned with the corresponding paired data. Consequently, these training-based approaches suffer from inherent *high costs* (*i.e.*, training and collecting paired data) and *limited generalization*.

Subsequent work resorts to training-free solutions that only modify the sampling process to achieve guided generation. There are two mainstream training-free strategies: 1) **Solving Inverse Problem** [5–7, 19, 21, 44]: As shown in Figure 2(b), instead of sampling from the marginal distribution, they approximate the posterior probability term and sample directly from the conditional distribution. However, the approximation used in these methods usually relies on a known forward fine-to-coarse operator, *i.e.*, the transformation from fine samples to coarse samples must be known, such as bicubic downsampling or a Gaussian mask operator. Thus, this prior (known operator) requirement reduces the robustness of these methods, as the operator may be unknown in many scenarios. 2) **Start-Guided Synthesis** [31, 41]: As shown in Figure 2(c), they first get the sampling start by adding noise to the coarse sample. Then they can sample from it with a pretrained diffusion model to get the refined sample. However, the guidance is entirely dependent on setting the noisy coarse sample as the starting point. Adding a large amount of noise results in loss of guidance signals, whereas adding a small amount of noise yields only limited quality improvement. In that

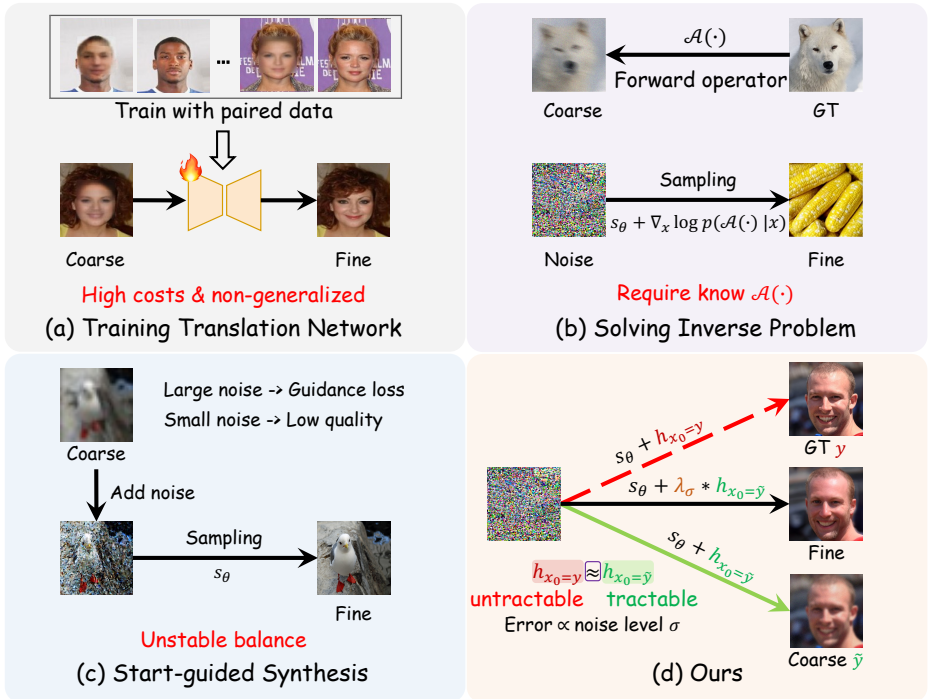


**Fig. 2: Existing and our solutions.** (a) Training translation networks based on paired data, which is costly and non-generalizable to different types of coarse samples. (b) Solving inverse problems based on a known forward operator, making it is not robust. (c) Adding noise to the coarse sample and denoising it, which is difficult to balance the guidance and quality. (d) Our method leverages the  $h$ -transform to achieve training-free, operator-free, and stable coarse-guided generation.

case, this start-dependent guided manner leads to an *unstable balance* between guidance faithfulness and generation quality.

Based on the above discussions, we observe that current solutions are constrained by training, the requirement for known operators, and unstable balance. To this end, inspired by Doob’s  $h$ -transform [10, 38], a tool that can constrain the sampling process with the given guidance, we propose a novel coarse-guided generation method **Weighted  $h$ -Transform Sampling**. Intuitively, our method incorporates guidance signals during sampling by modifying the transition probability at each time step and finally generates a guided refined result. This probability modification can be interpreted as introducing additional traction toward the *ideal underlying refined result* on top of the original sampling route.

Specifically, we achieve traction by adding a new drift adjustment  $h_{x_0=y}$  ( $x$  is the time-index updating latent and  $y$  is the ideal result) to the original predicted score  $s_\theta$  (cf., Figure 2(d)). By sampling with a new score ( $s_\theta + h_{x_0=y}$ ), the result can be guaranteed to be  $y$ . However, this  $h_{x_0=y}$  is not tractable because

it depends on knowing the ground truth, *i.e.*, ideal result  $\mathbf{y}$ . Since we can not directly get  $\mathbf{h}_{\mathbf{x}_0=\mathbf{y}}$ , we found that we can leverage another tractable  $\mathbf{h}_{\mathbf{x}_0=\tilde{\mathbf{y}}}$  to approximate it, where  $\tilde{\mathbf{y}}$  is the given coarse sample. Subsequently, we analyze the approximation error and find it to be negatively correlated with the noise level of  $\mathbf{x}$ . To mitigate the error influence, we use a noise-level-aware schedule to adjust the weight of  $\mathbf{h}_{\mathbf{x}_0=\tilde{\mathbf{y}}}$  across different time steps. That is, as the approximation error increases, we smoothly decrease the weight of the  $\mathbf{h}_{\mathbf{x}_0=\tilde{\mathbf{y}}}$  across the whole sampling process. In this way, the generated sample not only adheres to the coarse guidance but also improves in quality.

In summary, our contributions can be summarized as follows:

- We propose *Weighted h-Transform Sampling*, a coarse-guided visual generation method based on Doob’s *h*-transform perspective by deriving an approximation  $\mathbf{h}_{\mathbf{x}_0=\tilde{\mathbf{y}}}$  to replace the untractable  $\mathbf{h}_{\mathbf{x}_0=\mathbf{y}}$ . It is training-free, requires no prior knowledge of the forward operator, and is stable.
- We analyze the approximation error and indicate a negative correlation between the noise level and the approximation error. Then, we design a smooth, noise-level-aware weight schedule for the approximation term to mitigate the influence of approximation error.
- Extensive experiments across different image and video generation tasks show our effectiveness and generalization.

## 2 Background

### 2.1 Diffusion Models

The diffusion models aim to capture the target data distribution  $p_0$  by learning a transport process from a prior distribution  $p_T$  (*e.g.*, a Gaussian distribution) to  $p_0$ . To achieve that, a forward diffusion process from  $p_0$  to  $p_T$  is first determined and can be described with such a stochastic differential equation (SDE):

$$d\mathbf{x} = \mathbf{f}(\mathbf{x}_t, t)dt + g(t)d\mathbf{w}, \quad (1)$$

where  $t \in [0, T]$  is the time-index,  $\mathbf{x}_0 \sim p_0$ ,  $\mathbf{f}$  is the drift function,  $g$  is the diffusion coefficient, and  $\mathbf{w}$  is a Brown motion.

Meanwhile, the marginal distribution of  $\mathbf{x}_t$  at time  $t$  corresponding to this SDE is  $p_t(\mathbf{x}_t)$ . Then, we have a reversed SDE to describe the reversed process (from  $p_T$  to  $p_0$ ) of the forward process:

$$d\mathbf{x} = [\mathbf{f}(\mathbf{x}_t, t) - g^2(t)\nabla_{\mathbf{x}_t} \log p_t(\mathbf{x}_t)]dt + g(t)d\bar{\mathbf{w}}, \quad (2)$$

where  $\bar{\mathbf{w}}$  is the reversed Brown motion.

According to the Fokker–Planck equation [30] (F-P Equation), we can convert this reversed SDE into an ordinary differential equation (ODE) that has the same marginal distribution  $p_t(\mathbf{x}_t)$ :

$$d\mathbf{x} = [\mathbf{f}(\mathbf{x}_t, t) - \frac{1}{2}g^2(t)\nabla_{\mathbf{x}_t} \log p_t(\mathbf{x}_t)]dt. \quad (3)$$

We can sample synthetic samples by solving the SDE in Eq. (2) or the ODE in Eq. (3). However,  $\nabla_{\mathbf{x}_t} \log p_t(\mathbf{x}_t)$  (also known as the score) is not known. Thus, a parameterized network  $s_\theta(\cdot)$  with parameters  $\theta$  can be trained to predict it. The optimization target is:

$$\min_{\theta} \mathbb{E}_{\mathbf{x}_t, \mathbf{x}_0, t} [\|s_\theta(\mathbf{x}_t, t) - \nabla_{\mathbf{x}_t} \log p_t(\mathbf{x}_t | \mathbf{x}_0)\|_2^2], \quad (4)$$

where  $\mathbf{x}_0 \sim p_0$ ,  $t \in [0, T]$  and  $\mathbf{x}_t \sim p_t(\mathbf{x}_t | \mathbf{x}_0)$ .  $\nabla_{\mathbf{x}_t} \log p_t(\mathbf{x}_t | \mathbf{x}_0)$  are **tractable** since the conditional distribution is defined by the forward SDE in Eq. (1), and it has closed-form solutions. After training,  $s_\theta$  can be used as a score predictor to replace  $\nabla_{\mathbf{x}_t} \log p_t(\mathbf{x}_t)$  for solving Eq. (2) or Eq. (3).

## 2.2 Doob’s $h$ -Transform

For a given SDE like Eq. (1), the corresponding process can transport  $\mathbf{x}_0 \sim p_0$  to a Gaussian noise. However, in some situations, such as image translation, we may need to establish a mapping relation between  $\mathbf{x}_0$  and a fixed point  $\mathbf{y}$ . Thus, Doob’s  $h$ -transform [10, 38] proposes to modify the probability transition of the original SDE by adding an  $g^2(t)\mathbf{h}_{\mathbf{x}_T=\mathbf{y}}$  term to the original drifting term  $\mathbf{f}$ :

$$d\mathbf{x} = [\mathbf{f}(\mathbf{x}_t, t) + g^2(t)\mathbf{h}_{\mathbf{x}_T=\mathbf{y}}]dt + g(t)d\mathbf{w}, \quad (5)$$

where  $\mathbf{h}_{\mathbf{x}_T=\mathbf{y}}$  is called the  $h$  function. The new transition can guarantee that the SDE ends at the fixed point  $\mathbf{y}$ , where  $\mathbf{h}_{\mathbf{x}_T=\mathbf{y}}$  is designed as  $\nabla_{\mathbf{x}_t} \log p_t(\mathbf{x}_T = \mathbf{y} | \mathbf{x}_t)$ . It can improve the transition probability of  $p_t(\mathbf{x}_T = \mathbf{y} | \mathbf{x}_t)$  and guarantee  $\mathbf{x}_T = \mathbf{y}$  by adjusting the drift coefficient at each time step.

## 3 Weighted $h$ -Transform Sampling

**Problem Formulation.** Assuming that there exists an underlying joint distribution  $(\tilde{\mathbf{y}}, \mathbf{y}) \sim q$ , which describes the probability measurement between a coarse visual sample  $\tilde{\mathbf{y}}$  and its corresponding fine sample  $\mathbf{y}$ . For the coarse-guided visual generation task, given a coarse sample as the guidance  $\tilde{\mathbf{y}}$ , our objective is to leverage a pretrained diffusion model (*a.k.a.*, the score predictor)  $s_\theta$  to generate its corresponding fine sample.

### 3.1 Guided Generation with $h$ -Transform

For a given coarse sample  $\tilde{\mathbf{y}}$ , if we have its corresponding ideal fine sample  $\mathbf{y}$ , we can leverage the  $h$ -transform (*cf.*, Section 2.2) to modify the transition kernel of the reversed SDE (Eq. (2)) and guarantee it ends at  $\mathbf{y}$  (*i.e.*,  $\mathbf{x}_0 = \mathbf{y}$ ) by minusing<sup>1</sup>  $g^2(t)\mathbf{h}_{\mathbf{x}_0=\mathbf{y}}$  from the original drifting term:

$$d\mathbf{x} = [\mathbf{f}(\mathbf{x}_t, t) - g^2(t)\nabla_{\mathbf{x}_t} \log p_t(\mathbf{x}_t) - g^2(t)\mathbf{h}_{\mathbf{x}_0=\mathbf{y}}]dt + g(t)d\bar{\mathbf{w}}, \quad (6)$$

<sup>1</sup> Different from the adding in Eq. (5), here the minusing is because Eq. (2) is a reversed SDE, *i.e.*,  $dt < 0$ .

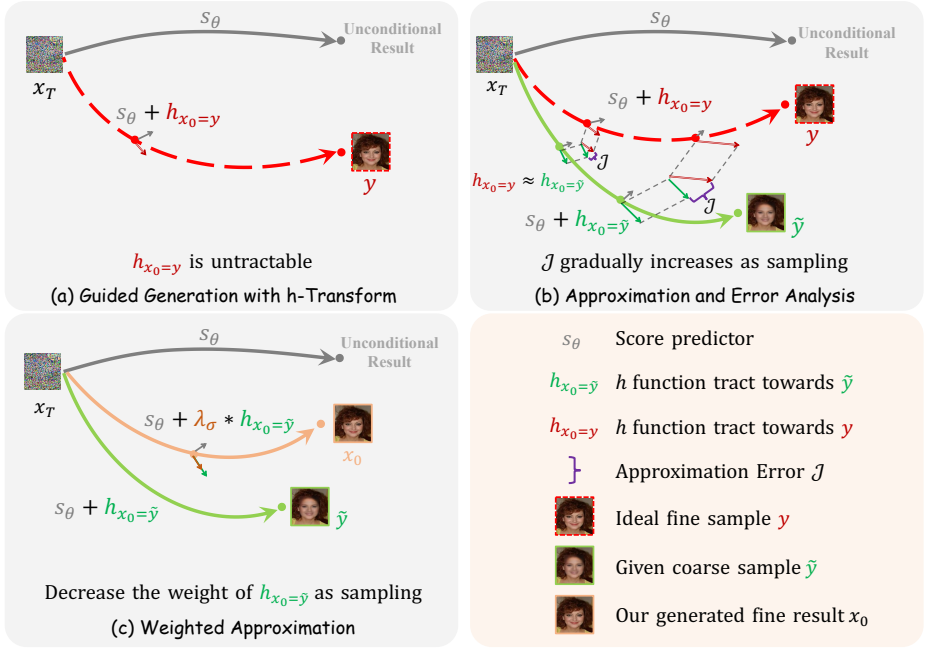


**Fig. 3: Overview of Weighted  $h$ -Transform Sampling.** (a) If we have  $h_{x_0=y}$ , the generation result will be the ideal sample. (b) We leverage  $h_{x_0=\tilde{y}}$  to approximate the untractable  $h_{x_0=y}$  and derive that the error is increasing gradually during the sampling process. (c) To mitigate the error influence, we decrease the approximation weight and finally generate a high-quality refined sample.

where  $h_{x_0=y}$  is  $\nabla_{x_t} \log p_t(x_0 = y | x_t)$ . For any  $x_T$ , after solving this SDE, the endpoint  $x_0$  must be  $y$  (shown in Figure 3(a)). To simplify the solving process, we can further convert Eq. (6) into its corresponding PF-ODE:

$$dx = [f(x_t, t) - \frac{1}{2}g^2(t)(\nabla_{x_t} \log p_t(x_t) + h_{x_0=y})]dt. \quad (7)$$

This ODE has the equivalent marginal distribution as Eq. (6)<sup>2</sup>. Thus, the solution of Eq. (7) is also  $y$ . However, it's obvious that the  $h_{x_0=y}$  is not known since  $y$  is off-course unknown as the ground truth we want to generate. Thus, we can not directly achieve the guided generation using Eq. (7).

### 3.2 Approximation for the Untractable $h_{x_0=y}$

As  $h_{x_0=y} = \nabla_{x_t} \log p_t(x_0 = y | x_t)$  is untractable, we manage to convert it into a tractable and appropriate approximation. To this end, we propose to approximate it with the following:

$$h_{x_0=y} = \nabla_{x_t} \log p_t(x_0 = y | x_t) \approx \nabla_{x_t} \log p_t(x_0 = \tilde{y} | x_t). \quad (8)$$

<sup>2</sup> This can be proved by the F-P Equation, and we provide the proof in the Appendix.

We name  $\nabla_{\mathbf{x}_t} \log p_t(\mathbf{x}_0 = \tilde{\mathbf{y}}|\mathbf{x}_t)$  as  $\mathbf{h}_{\mathbf{x}_0=\tilde{\mathbf{y}}}$ , which is another  $h$  function (cf., Figure 3(b)). Then, we use Bayes' rule to change  $\mathbf{h}_{\mathbf{x}_0=\tilde{\mathbf{y}}}$  into:

$$\begin{aligned} \mathbf{h}_{\mathbf{x}_0=\tilde{\mathbf{y}}} &= \nabla_{\mathbf{x}_t} \log p_t(\mathbf{x}_0 = \tilde{\mathbf{y}}|\mathbf{x}_t) \\ &= \nabla_{\mathbf{x}_t} \log p_t(\mathbf{x}_t|\mathbf{x}_0 = \tilde{\mathbf{y}}) - \nabla_{\mathbf{x}_t} \log p_t(\mathbf{x}_t), \end{aligned} \quad (9)$$

where the second term  $\nabla_{\mathbf{x}_t} \log p_t(\mathbf{x}_t)$  can be replaced by the given trained score predictor  $s_\theta$ . Besides, we already known the conditional distribution  $p_t(\mathbf{x}_t|\mathbf{x}_0)$ :

$$p_t(\mathbf{x}_t|\mathbf{x}_0) = \mathcal{N}(\mathbf{x}_t; \alpha_t \mathbf{x}_0, \sigma_t^2 \mathbf{I}), \quad (10)$$

where  $\alpha_t$  and  $\sigma_t$  (noise level) are determined by  $\mathbf{f}(\mathbf{x}_t, t)$ ,  $g^2(t)$  of Eq. (1). When  $\mathbf{x}_0 = \tilde{\mathbf{y}}$ , which is also given as the coarse sample,  $p_t(\mathbf{x}_t|\mathbf{x}_0 = \tilde{\mathbf{y}})$  is closed-form as  $\mathcal{N}(\mathbf{x}_t; \alpha_t \tilde{\mathbf{y}}, \sigma_t^2 \mathbf{I})$  and  $\nabla_{\mathbf{x}} \log p_t(\mathbf{x}_t|\mathbf{x}_0 = \tilde{\mathbf{y}})$  is tractable:

$$\begin{aligned} \nabla_{\mathbf{x}} \log p_t(\mathbf{x}_t|\mathbf{x}_0 = \tilde{\mathbf{y}}) &= \nabla_{\mathbf{x}_t} \left( -\frac{1}{2\sigma_t^2} (\mathbf{x}_t - \alpha_t \tilde{\mathbf{y}})^{\mathbf{T}} (\mathbf{x}_t - \alpha_t \tilde{\mathbf{y}}) \right) \\ &= \frac{1}{\sigma_t^2} (\alpha_t \tilde{\mathbf{y}} - \mathbf{x}_t). \end{aligned} \quad (11)$$

After that, we achieve to convert the untractable  $\mathbf{h}_{\mathbf{x}_0=\mathbf{y}}$  into the following tractable approximation:

$$\mathbf{h}_{\mathbf{x}_0=\mathbf{y}} \approx \mathbf{h}_{\mathbf{x}_0=\tilde{\mathbf{y}}} = \frac{1}{\sigma_t^2} (\alpha_t \tilde{\mathbf{y}} - \mathbf{x}_t) - \nabla_{\mathbf{x}_t} \log p_t(\mathbf{x}_t). \quad (12)$$

### 3.3 Approximation Error Analysis

Our proposed approximation in Eq. (8) inevitably introduces approximation errors. We can calculate the Euclidean distance between  $\mathbf{h}_{\mathbf{x}_0=\mathbf{y}}$  and  $\mathbf{h}_{\mathbf{x}_0=\tilde{\mathbf{y}}}$  as the approximation error  $\mathcal{J}$ :

$$\begin{aligned} \mathcal{J} &= \|\nabla_{\mathbf{x}} \log p_t(\mathbf{x}_0 = \mathbf{y}|\mathbf{x}_t) - \nabla_{\mathbf{x}} \log p_t(\mathbf{x}_0 = \tilde{\mathbf{y}}|\mathbf{x}_t)\|_2 \\ &= \|\nabla_{\mathbf{x}} \log p_t(\mathbf{x}_t|\mathbf{x}_0 = \tilde{\mathbf{y}}) - \nabla_{\mathbf{x}} \log p_t(\mathbf{x}_t|\mathbf{x}_0 = \mathbf{y})\|_2 \\ &= \left\| \frac{\alpha_t}{\sigma_t^2} (\tilde{\mathbf{y}} - \mathbf{y}) \right\|_2. \end{aligned} \quad (13)$$

Taking the variance-preserving (VP) diffusion model as the example ( $\alpha_t^2 + \sigma_t^2 = 1$ ), we can replace  $\alpha_t$  with  $\sigma$  in Eq. (13) and get:

$$\mathcal{J} = \left\| \frac{\sqrt{(1 - \sigma_t^2)}}{\sigma_t^2} (\tilde{\mathbf{y}} - \mathbf{y}) \right\|_2. \quad (14)$$

We can see that the approximation error  $\mathcal{J}$  is negatively correlated with the noise level  $\sigma_t$ . Meanwhile, when  $\sigma_t \rightarrow 0$ ,  $\mathcal{J} \rightarrow \infty$  and when  $\sigma_t \rightarrow 1$ ,  $\mathcal{J} \rightarrow 0$ .

---

**Algorithm 1** Weighted  $h$ -Transform Sampling
 

---

- 1: **Input:** Coarse visual sample  $\tilde{\mathbf{y}}$ , Pretrained score predictor  $s_\theta$ , Step number  $M$ , Step size  $\Delta_t$ , Noise schedules  $\alpha_t$  and  $\sigma_t^2$ , Weight function  $\lambda_\sigma$
  - 2: **Output:** Refined synthetic sample  $\mathbf{x}_0$
  - 3:  $t = T$
  - 4:  $\mathbf{x}_t \sim \mathcal{N}(0, \mathbf{I})$
  - 5: **for**  $n = M$  to 1 **do**
  - 6:    $\mathbf{x}_{t-\Delta_t} = \mathbf{x}_t - [\mathbf{f}(\mathbf{x}_t, t) - \frac{1}{2}g^2(t)(s_\theta + \lambda_\sigma * (\frac{1}{\sigma_t^2}(\alpha_t\tilde{\mathbf{y}} - \mathbf{x}_t) - s_\theta))]\Delta_t$
  - 7:    $t = t - \Delta_t$
  - 8: **end for**
- 

### 3.4 Weighted Approximation for Error Restriction

According to Eq. (12), we can directly substitute this approximation into the sampling ODE Eq. (7) to get the guided generation result. However, as we discussed in Section 3.3, the approximation error will gradually become unbearable during the sampling process (as  $\sigma_t$  is getting smaller gradually).

To this end, we manage to design a weight function for the approximated part to mitigate the influence of the approximation error. When the approximation error is small, the weight can be close to 1. Otherwise, the weight should be decreased gradually to 0. Exactly, we found the noise level  $\sigma_t$  has a good property that satisfies the weight design requirement. Thus, as shown in Figure 3(c), we can use a  $\sigma_t$ -related weight function to adjust the approximation term and get the final sampling ODE:

$$d\mathbf{x} = [\mathbf{f}(\mathbf{x}_t, t) - \frac{1}{2}g^2(t)(s_\theta + \lambda_\sigma * (\frac{1}{\sigma_t^2}(\alpha_t\tilde{\mathbf{y}} - \mathbf{x}_t) - s_\theta))]dt, \quad (15)$$

where  $\lambda_\sigma$  is a function of  $\sigma_t$  (*e.g.*, a power function) such that: (1)  $\lambda_\sigma$  is negatively correlated with  $\mathcal{J}$ . (2)  $\lambda_\sigma \rightarrow 1$  when  $\mathcal{J} \rightarrow 0$ . (3)  $\lambda_\sigma \rightarrow 0$  when  $\mathcal{J} \rightarrow \infty$ .

Intuitively, the  $\mathbf{h}_{\mathbf{x}_0=\mathbf{y}}$  term can drag the sampling path towards the ideal sample  $\mathbf{y}$ . However, the  $\mathbf{h}_{\mathbf{x}_0=\mathbf{y}}$  term is untractable, so we use an  $\mathbf{h}_{\mathbf{x}_0=\tilde{\mathbf{y}}}$  to approximate it. When the approximation error is small, the traction towards  $\mathbf{y}$  is accurate, so we adopt the approximated  $\mathbf{h}_{\mathbf{x}_0=\tilde{\mathbf{y}}}$  term more. Otherwise, traction towards  $\mathbf{y}$  is inaccurate, so we adopt the approximated  $\mathbf{h}_{\mathbf{x}_0=\tilde{\mathbf{y}}}$  term a little. Finally, our overall sampling algorithm (take the Euler Solver as an example) is shown in Algorithm 1.

## 4 Related Work

**Diffusion Models and Bridges.** Diffusion models have recently achieved state-of-the-art visual modeling capability. Although DDPM [14,42], Score matching [43,44], and Optimal-transport Flow matching [27,28] provide different perspectives to understand the diffusion family, their success mainly comes from the progressive transport between a prior distribution and the target distribution.

Based on these techniques, various large-scale pre-trained diffusion models, such as Stable Diffusion [11, 35, 39], Flux [23, 24], and Wan [49] have emerged and demonstrated remarkable generative performance. In addition to noise-to-visual generation, some works [8, 45, 58, 59] propose diffusion bridges to achieve the visual-to-visual translations. The most typical paradigm is leveraging Doob’s  $h$ -transform [10, 38] to link the paired samples and learn a joint distribution to transport between them. Our paper is inspired by the  $h$ -transform technique that modifies the probability transition to achieve the guided visual generation.

**Conditional Visual Generation.** Compared with unconditional generation, the conditional generation [1, 15, 55] aims to handle various modality conditions (*e.g.*, text, action, and visual samples) as guidance to constrain the generation range. The text condition is easy to model due to the large-scale text-visual pairs. To this end, current research around conditional generation mainly indicates that the condition is some types of visual signals (*e.g.*, coarse sample, stroke, and pose map). Based on different condition types, the task can be specified into image restoration [25, 37, 51], inverse problem [5, 6, 21, 46], and conditional control [40, 56], and so on. Meanwhile, the solutions also contain training-based [32, 34, 50] and inference-stage guidance [12, 54]. In our paper, we mainly focus on the conditional generation with coarse samples as guidance and generate corresponding high-quality fine samples in a training-free manner.

## 5 Experiments

### 5.1 Coarse-Image Guided Generation

To demonstrate our effectiveness, we first evaluated on image restoration tasks, a fundamental challenge in computer vision that aims to recover high-quality original scenes from degraded, noisy, or incomplete coarse samples. Specifically, this task entails recovering a clean image  $\mathbf{y}$  based on a given coarse image  $\tilde{\mathbf{y}}$ .

**Benchmark.** Following DPS [6], we use the validation set of FFHQ 256x256 [18] to serve as the evaluation dataset. This dataset contains 1000 clean images of human faces in  $256 * 256$  resolution. For the evaluation metrics, we adopt Frechet Inception Distance [13] ( $FID$ ) and Learned Perceptual Image Patch Similarity [57] ( $LPIPS$ ) to quantify the effectiveness.  $FID$  can indicate the distribution similarity between synthetic images and ground-truth images, while  $LPIPS$  focuses on image-level similarity.

**Implementations.** Following the protocol in DPS [6], we transform all clean images  $\mathbf{y}$  by using a forward operator  $\mathcal{A}$  and additive noise  $\mathbf{n}$  into coarse images  $\tilde{\mathbf{y}}$ , *i.e.*,  $\tilde{\mathbf{y}} = \mathcal{A}(\mathbf{y}) + \mathbf{n}$ . Depending on different forward operators, it can be divided into four image restoration tasks: super-resolution ( $SR$ ), inpainting ( $Inpaint$ ), motion deblur ( $MD$ ), and Gaussian deblur ( $GD$ ). These coarse images  $\tilde{\mathbf{y}}$  serve as the guidance in the subsequent generation process. For fair comparison, we follow previous work [6] and use the same pre-trained diffusion model from [9] and

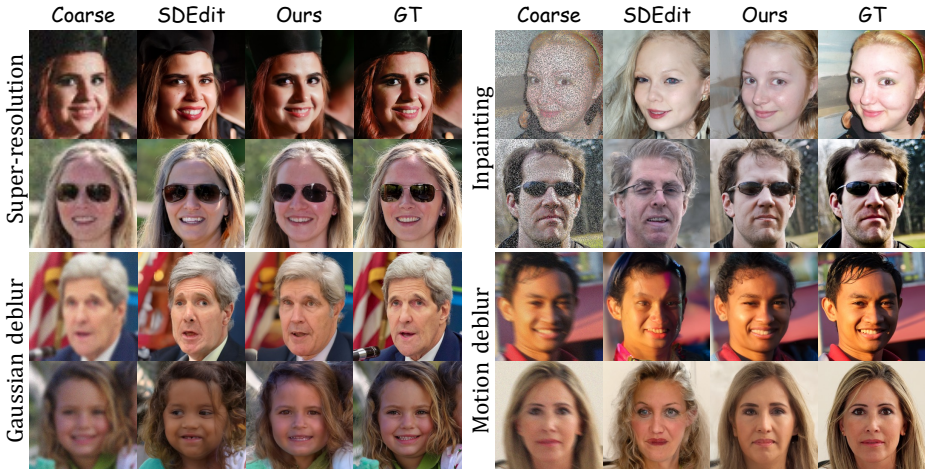


**Fig. 4: Qualitative results of coarse-guided image generation.** Compared with training-free SDEdit, our method shows more faithful synthesis across tasks. For fairness, we take their own commonly-used hyper-parameter for SDEdit ( $t_0 = 500$ ) and ours ( $\alpha = 5$ ), and all other settings are the same.

maintain other settings the same. During sampling, we set the weight function  $\lambda_\sigma = \sigma^\alpha$  and report the average result on  $\alpha \in \{5, 6, 7\}$ .

**Baselines.** We compared our method against: 1) six inverse-problem solutions (*cf.*, Figure 2(b)): ADMM-TV, ILVR [5, 44], PnP-ADMM [4], MCG [7], DDRM [19], and DPS [6]. These solutions require additional prior for knowing the forward operator. We report their results from [6]. 2) The represented start-guided solution (*cf.*, Figure 2(c)): SDEdit [31], which does not require knowing the forward operator. It has a key hyperparameter: the starting timestep  $t_0$ , which can control the tradeoff between guidance and synthesis quality. For fairness, we report the results averaged on three recommended  $t_0$  from the original paper, *i.e.*,  $t_0 \in \{400, 500, 600\}$ , and keep all other settings the same.

**Results.** We gave quantitative comparisons in Table 1. We can see that: 1) Compared with operator-required methods, our approach can outperform most of them and perform competitively against their best one, *i.e.*, DPS. It’s worth noting that we achieve it without knowing the forward operator, which is a strong prior. 2) Compared with SDEdit, our method can outperform it across six of eight metrics, particularly yielding substantial and consistent improvements in *LPIPS*. This verifies that our Weighted *h*-Transform Sampling provides a more robust and principled mechanism for coarse-image guidance, leading to superior structural preservation and fidelity. We also gave qualitative comparisons in Figure 4. We can see that our results show a better balance between the guidance adherence and image quality than SDEdit.

**Table 1:** Quantitative results of coarse-image guided generation on FFHQ 256x256 validation dataset. **Bold:** best, underline: second best.

Method	Known Operator	SR		Inpaint		GD		MD	
		FID $\downarrow$	LPIPS $\downarrow$						
ADMM-TV	✓	110.6	0.428	181.5	0.463	186.7	0.507	152.3	0.508
ILVR [5, 44]	✓	96.72	0.563	76.54	0.612	109.0	0.403	292.2	0.657
PnP-ADMM [4]	✓	66.52	0.353	123.6	0.692	90.42	0.441	89.08	0.405
MCG [7]	✓	87.64	0.520	<u>29.26</u>	0.286	101.2	0.340	310.5	0.702
DDRM [19]	✓	62.15	0.294	69.71	0.587	74.92	0.332	-	-
DPS [6]	✓	39.35	<u>0.214</u>	<b>21.19</b>	<b>0.212</b>	44.05	<u>0.257</u>	<b>39.92</b>	<b>0.242</b>
SDEdit [31]		<u>33.31</u>	0.269	47.24	0.390	<b>34.90</b>	0.291	<u>42.35</u>	0.350
<b>Ours</b>		<b>33.28</b>	<b>0.213</b>	44.64	<u>0.259</u>	<u>38.05</u>	<b>0.252</b>	52.92	<u>0.341</u>

**Table 2:** Quantitative results of camera-controlled video generation on DL3DV.

Method	MSE $\downarrow$	LPIPS $\downarrow$	FVD $\downarrow$	DINOv2 $\downarrow$	CLIP Cons. $\uparrow$	Optical Flow $\downarrow$
GT	-	-	-	-	0.974	-
Coarse Video	11.46	0.276	15.55	0.220	0.973	41.3
GWTF( $\gamma = 0.5$ )	26.08	0.360	15.31	0.149	0.975	118.5
GWTF( $\gamma = 0.7$ )	36.45	0.457	21.25	0.173	<b>0.984</b>	145.2
TTM( $t_w = 4, t_s = 8$ )	23.50	0.382	15.69	0.147	0.980	157.2
TTM( $t_w = 4, t_s = 9$ )	23.15	0.380	15.59	0.147	0.980	158.8
<b>Ours</b>	<b>11.45</b>	<b>0.272</b>	<b>13.26</b>	<b>0.143</b>	0.972	<b>38.7</b>

## 5.2 Coarse-Video Guided Generation

To further verify the effectiveness and generalization of our method, we leverage it to achieve camera-controlled video generation by treating this task as a coarse-video guided generation process. The camera-controlled video generation is: given the first frame, corresponding camera intrinsics, and the pose, we aim to generate a video that follows a sequence of prescribed camera motions. To achieve this, we first use pretrained 3-D models to render a coarse video from the first frame and the prescribed camera motions. This coarse video is low-quality (warped) but can capture camera motion. Then it will serve as the guidance for the subsequent video generation.

**Dataset.** Following previous camera-controlled video generation work, we use DL3DV-10K [26] as our dataset for constructing coarse videos and for evaluation. DL3DV-10K contains annotated data samples, each comprising a video with camera intrinsics and camera poses of all frames. We randomly select 160 samples, retain the first 49 frames, and resize them to  $720 * 480$  resolution. We use this subset as our dataset.

**Implementations.** We first use DepthPro [2] to extract the depth information of the first frame. Then project it into a 3-D point cloud. For the given sequenced



**Fig. 5: Qualitative comparisons on the subset of DL3DV-10K.** Our method shows better appearance alignment to the ground truth (see highlighted blue boxes).

camera motion poses, we can render a sequence of corresponding images and concatenate them into the coarse video. The coarse video contains two parts. 1) Valid part: pixels that exist in the given first frame. 2) Invalid part: Pixels that do not exist in the given first frame. For the invalid part, the pixels are filled by nearest-neighbor assignment. All details about obtaining the coarse video are in the Appendix. During sampling, we set the weight function  $\lambda_\sigma = \sigma^\alpha$  and give these two parts different  $\alpha$ . For the valid part,  $\alpha = 4$  and for the invalid part,  $\alpha = 8$ . The pretrained model we used is CogVideoX-5b-I2V [53]. For all other hyperparameters, we followed the default settings of previous work [41, 53].

**Baselines.** We compared our method with 1) Training-based GWTF [3]: learning a noise warping based on optical flows to model the motion. We used the official trained model and set its key hyper-parameter degradation value  $\gamma$  to 0.5 and 0.7 as recommended in the original paper. 2) Training-free TTM [41]: leverage start-guided synthesis for two decoupled parts. This method also depends on a coarse video. For fairness, we use the same warped coarse as ours. We also took  $t_{weak} = 4$  ( $t_w$ ),  $t_{strong} = 8$  ( $t_s$ ), and  $t_{weak} = 4$ ,  $t_{strong} = 9$  according to the default and recommended in their paper and code. For all other hyperparameters, we follow their default or recommendations.

**Metrics.** We evaluated the quality of generated videos at the frame level using Mean Squared Error (*MSE*) and *LPIPS* [57] relative to the ground-truth videos. Additionally, we calculated the distributional difference between the ground-truth videos and the synthetic videos using Frechet Video Distance [48] (*FVD*). We also calculated the average semantic similarity of each frame between ground-truth videos and the synthetic videos with DINOv2 Distance [33] (*DINOv2*). We used the CLIP similarity [36] between two consistent frames (*CLIP Cons.*) to evaluate the temporal consistency. For camera motion consistency, we calculated the Mean Squared Error between the RAFT-estimated optical flows [47] of the ground-truth videos and those of the synthetic videos (*Optical Flow*).

**Results.** As shown in Table 2, our method achieves the best performance across all metrics except *CLIP Cons.*. This indicates that our synthetic videos are closest to ground-truth videos and have the best motion consistency. For the *CLIP Cons.*, although our method has the lowest 0.972, we should note that the ground truth only achieves 0.974 on this metric. This indicates that other methods even outperform the ground truth on this metric by sacrificing motion consistency to get quite similar consecutive frames. Additionally, we provide qualitative comparisons in Figure 5. We can see that our method can generate videos with better ground truth alignment and decent image quality. This indicates that our method can effectively generate high-quality videos under coarse video guidance.

### 5.3 Ablation on Hyperparameter $\alpha$

Since the weight scheduler  $\lambda_\sigma = \sigma_t^\alpha$ , the weight of the  $h$  term can be adjusted by  $\alpha$ . To investigate the impact of this key hyperparameter, we ablated it on the super-resolution task (same setting as Section 5.1). For  $\alpha \in \{1, 3, 5, 7, 9\}$ , we report the change curves of *FID* and *LPIPS* in Figure 6. When the  $\alpha$  is small (*e.g.*, 1), the corresponding weight is large and incorporates an unbearable approximation error. Thus, we can observe that both

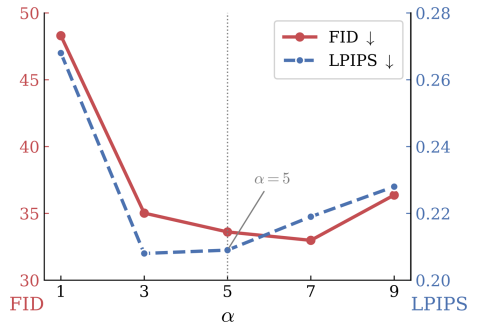


Fig. 6: Ablation study of the  $\alpha$ .

metrics are quite high. As the  $\alpha$  increases, the performance improves since the error is restricted effectively and achieves a good performance around  $\alpha = 5$ . After that, performance again degraded due to the insufficient traction from a small weighted  $h$ . Moreover, we also provided the visualizations of synthetic results under various  $\alpha$  in Figure 7. We can see that when  $\alpha$  is too small (*e.g.*, 1), the image quality is limited (not clear) due to a large approximation error. When  $\alpha$  is excessively large (*e.g.*, 9), the synthetic image deviates from the ground-truth due to the insufficient guidance of the coarse image. When the  $\alpha$  is tempered (*e.g.*, around 5), our method achieves a good balance between image quality and guidance adherence. More ablations are in the Appendix.



**Fig. 7: Super-resolution results by using different  $\alpha$ .** A large  $\alpha$  leads to a small weight, and vice versa (weight scheduler  $\lambda_\sigma = \sigma_t^\alpha$ ).

## 5.4 Compatibility with Flow Matching Models

To further verify the generalization ability of our method, we evaluated it on the camera-controlled video generation task (*cf.*, Section 5.2) by using a flow-based model Wan2.2 [49]. We gave qualitative results of Wan2.2 in Figure 8. We can observe that when the pretrained model is Wan2.2, the synthetic videos also yield a decent synthetic result (even better than CogVideoX since Wan2.2 is a stronger base



**Fig. 8: Our method is compatible with both score-based CogVideoX and Flow-based Wan2.2.**

model) under the guidance of the coarse video. This indicates that our method is compatible with both score-based models like CogVideoX and flow-based models like Wan2.2, showing good generalizations. This indicates that, although our proposed Weighted  $h$ -Transform Sampling is based on the score perspective, it can generally be compatible with flow matching and score matching.

## 6 Conclusion

In this paper, we proposed **Weighted  $h$ -Transform Sampling** for coarse-guided visual generation. We inject the guidance during the sampling process by designing an  $h$  function that can approximately drive the generation towards the underlying ideal sample. We further design a weight scheduler to restrict the approximation error for better synthetic results. Extensive comparisons and ablation show the generalizations and effectiveness. In the future, probability transition modification mechanisms (represented by  $h$ -transform) can be further explored in more general conditional generation applications.

## References

1. Batzolis, G., Stanczuk, J., Schönlieb, C.B., Etmann, C.: Conditional image generation with score-based diffusion models. arXiv preprint arXiv:2111.13606 (2021)
2. Bochkovskii, A., Delaunoy, A., Germain, H., Santos, M., Zhou, Y., Richter, S.R., Koltun, V.: Depth pro: Sharp monocular metric depth in less than a second. arXiv preprint arXiv:2410.02073 (2024)
3. Burgert, R., Xu, Y., Xian, W., Pilarski, O., Clausen, P., He, M., Ma, L., Deng, Y., Li, L., Mousavi, M., et al.: Go-with-the-flow: Motion-controllable video diffusion models using real-time warped noise. In: Proceedings of the Computer Vision and Pattern Recognition Conference. pp. 13–23 (2025)
4. Chan, S.H., Wang, X., Elgendy, O.A.: Plug-and-play admm for image restoration: Fixed-point convergence and applications. IEEE Transactions on Computational Imaging **3**(1), 84–98 (2016)
5. Choi, J., Kim, S., Jeong, Y., Gwon, Y., Yoon, S.: Ilvr: Conditioning method for denoising diffusion probabilistic models. arXiv preprint arXiv:2108.02938 (2021)
6. Chung, H., Kim, J., Mccann, M.T., Klasky, M.L., Ye, J.C.: Diffusion posterior sampling for general noisy inverse problems. arXiv preprint arXiv:2209.14687 (2022)
7. Chung, H., Sim, B., Ryu, D., Ye, J.C.: Improving diffusion models for inverse problems using manifold constraints. Advances in Neural Information Processing Systems **35**, 25683–25696 (2022)
8. De Bortoli, V., Thornton, J., Heng, J., Doucet, A.: Diffusion schrödinger bridge with applications to score-based generative modeling. Advances in neural information processing systems **34**, 17695–17709 (2021)
9. Dhariwal, P., Nichol, A.: Diffusion models beat gans on image synthesis. Advances in neural information processing systems **34**, 8780–8794 (2021)
10. Doob, J.L., Doob, J.: Classical potential theory and its probabilistic counterpart, vol. 262. Springer (1984)
11. Esser, P., Kulal, S., Blattmann, A., Entezari, R., Müller, J., Saini, H., Levi, Y., Lorenz, D., Sauer, A., Boesel, F., et al.: Scaling rectified flow transformers for high-resolution image synthesis. In: Forty-first international conference on machine learning (2024)
12. Gao, Z., Song, J., Zhang, Z., Deng, J., Patras, I.: Frequency-guided diffusion for training-free text-driven image translation. In: Proceedings of the IEEE/CVF International Conference on Computer Vision. pp. 19195–19205 (2025)
13. Heusel, M., Ramsauer, H., Unterthiner, T., Nessler, B., Hochreiter, S.: Gans trained by a two time-scale update rule converge to a local nash equilibrium. Advances in neural information processing systems **30** (2017)
14. Ho, J., Jain, A., Abbeel, P.: Denoising diffusion probabilistic models. Advances in neural information processing systems **33**, 6840–6851 (2020)
15. Ho, J., Salimans, T.: Classifier-free diffusion guidance. arXiv preprint arXiv:2207.12598 (2022)
16. Hurst, A., Lerer, A., Goucher, A.P., Perelman, A., Ramesh, A., Clark, A., Ostrow, A., Welihinda, A., Hayes, A., Radford, A., et al.: Gpt-4o system card. arXiv preprint arXiv:2410.21276 (2024)
17. Ju, X., Zeng, A., Bian, Y., Liu, S., Xu, Q.: Pnp inversion: Boosting diffusion-based editing with 3 lines of code. In: The Twelfth International Conference on Learning Representations (2023)
18. Karras, T., Laine, S., Aila, T.: A style-based generator architecture for generative adversarial networks. In: Proceedings of the IEEE/CVF conference on computer vision and pattern recognition. pp. 4401–4410 (2019)

19. Kawar, B., Elad, M., Ermon, S., Song, J.: Denoising diffusion restoration models. *Advances in neural information processing systems* **35**, 23593–23606 (2022)
20. Kim, J., Hong, Y., Ye, J.C.: Flowalign: Trajectory-regularized, inversion-free flow-based image editing. *arXiv preprint arXiv:2505.23145* (2025)
21. Kim, J., Kim, B.S., Ye, J.C.: Flowdps: Flow-driven posterior sampling for inverse problems. *arXiv preprint arXiv:2503.08136* (2025)
22. Kulikov, V., Kleiner, M., Huberman-Spiegelglas, I., Michaeli, T.: Flowedit: Inversion-free text-based editing using pre-trained flow models. *arXiv preprint arXiv:2412.08629* (2024)
23. Labs, B.F.: Flux. <https://github.com/black-forest-labs/flux> (2024)
24. Labs, B.F., Batifol, S., Blattmann, A., Boesel, F., Consul, S., Diagne, C., Dockhorn, T., English, J., English, Z., Esser, P., et al.: Flux. 1 kontext: Flow matching for in-context image generation and editing in latent space. *arXiv preprint arXiv:2506.15742* (2025)
25. Liang, J., Cao, J., Sun, G., Zhang, K., Van Gool, L., Timofte, R.: Swinir: Image restoration using swin transformer. In: *Proceedings of the IEEE/CVF international conference on computer vision*. pp. 1833–1844 (2021)
26. Ling, L., Sheng, Y., Tu, Z., Zhao, W., Xin, C., Wan, K., Yu, L., Guo, Q., Yu, Z., Lu, Y., et al.: D13d-10k: A large-scale scene dataset for deep learning-based 3d vision. In: *Proceedings of the IEEE/CVF Conference on Computer Vision and Pattern Recognition*. pp. 22160–22169 (2024)
27. Lipman, Y., Chen, R.T., Ben-Hamu, H., Nickel, M., Le, M.: Flow matching for generative modeling. *arXiv preprint arXiv:2210.02747* (2022)
28. Liu, X., Gong, C., Liu, Q.: Flow straight and fast: Learning to generate and transfer data with rectified flow. *arXiv preprint arXiv:2209.03003* (2022)
29. Lowe, D.G.: Distinctive image features from scale-invariant keypoints. *International journal of computer vision* **60**(2), 91–110 (2004)
30. Maoutsa, D., Reich, S., Opper, M.: Interacting particle solutions of fokker–planck equations through gradient–log–density estimation. *Entropy* **22**(8), 802 (2020)
31. Meng, C., Song, Y., Song, J., Wu, J., Zhu, J.Y., Ermon, S.: Sdedit: Image synthesis and editing with stochastic differential equations. *arXiv preprint arXiv:2108.01073* (2021)
32. Murez, Z., Kolouri, S., Kriegman, D., Ramamoorthi, R., Kim, K.: Image to image translation for domain adaptation. In: *Proceedings of the IEEE conference on computer vision and pattern recognition*. pp. 4500–4509 (2018)
33. Oquab, M., Darcet, T., Moutakanni, T., Vo, H., Szafraniec, M., Khalidov, V., Fernandez, P., Haziza, D., Massa, F., El-Nouby, A., et al.: Dinov2: Learning robust visual features without supervision. *arXiv preprint arXiv:2304.07193* (2023)
34. Parmar, G., Park, T., Narasimhan, S., Zhu, J.Y.: One-step image translation with text-to-image models. *arXiv preprint arXiv:2403.12036* (2024)
35. Podell, D., English, Z., Lacey, K., Blattmann, A., Dockhorn, T., Müller, J., Penna, J., Rombach, R.: Sdxl: Improving latent diffusion models for high-resolution image synthesis. *arXiv preprint arXiv:2307.01952* (2023)
36. Radford, A., Kim, J.W., Hallacy, C., Ramesh, A., Goh, G., Agarwal, S., Sastry, G., Askell, A., Mishkin, P., Clark, J., et al.: Learning transferable visual models from natural language supervision. In: *International conference on machine learning*. pp. 8748–8763. Pmlr (2021)
37. Ren, M., Delbraccio, M., Talebi, H., Gerig, G., Milanfar, P.: Multiscale structure guided diffusion for image deblurring. In: *Proceedings of the IEEE/CVF international conference on computer vision*. pp. 10721–10733 (2023)

38. Rogers, L.C.G., Williams, D.: *Diffusions, Markov processes, and martingales*, vol. 2. Cambridge university press (2000)
39. Rombach, R., Blattmann, A., Lorenz, D., Esser, P., Ommer, B.: High-resolution image synthesis with latent diffusion models. In: *Proceedings of the IEEE/CVF conference on computer vision and pattern recognition*. pp. 10684–10695 (2022)
40. Shen, F., Tang, J.: Imagpose: A unified conditional framework for pose-guided person generation. *Advances in neural information processing systems* **37**, 6246–6266 (2024)
41. Singer, A., Rotstein, N., Mann, A., Kimmel, R., Litany, O.: Time-to-move: Training-free motion controlled video generation via dual-clock denoising. *arXiv preprint arXiv:2511.08633* (2025)
42. Song, J., Meng, C., Ermon, S.: Denoising diffusion implicit models. *arXiv preprint arXiv:2010.02502* (2020)
43. Song, Y., Ermon, S.: Generative modeling by estimating gradients of the data distribution. *Advances in neural information processing systems* **32** (2019)
44. Song, Y., Sohl-Dickstein, J., Kingma, D.P., Kumar, A., Ermon, S., Poole, B.: Score-based generative modeling through stochastic differential equations. *arXiv preprint arXiv:2011.13456* (2020)
45. Su, X., Song, J., Meng, C., Ermon, S.: Dual diffusion implicit bridges for image-to-image translation. *arXiv preprint arXiv:2203.08382* (2022)
46. Tarantola, A.: *Inverse problem theory and methods for model parameter estimation*. SIAM (2005)
47. Teed, Z., Deng, J.: Raft: Recurrent all-pairs field transforms for optical flow. In: *European conference on computer vision*. pp. 402–419. Springer (2020)
48. Unterthiner, T., Van Steenkiste, S., Kurach, K., Marinier, R., Michalski, M., Gelly, S.: Towards accurate generative models of video: A new metric & challenges. *arXiv preprint arXiv:1812.01717* (2018)
49. Wan, T., Wang, A., Ai, B., Wen, B., Mao, C., Xie, C.W., Chen, D., Yu, F., Zhao, H., Yang, J., et al.: Wan: Open and advanced large-scale video generative models. *arXiv preprint arXiv:2503.20314* (2025)
50. Wang, T., Zhang, T., Zhang, B., Ouyang, H., Chen, D., Chen, Q., Wen, F.: Pretraining is all you need for image-to-image translation. *arXiv preprint arXiv:2205.12952* (2022)
51. Wang, Z., Chen, J., Hoi, S.C.: Deep learning for image super-resolution: A survey. *IEEE transactions on pattern analysis and machine intelligence* **43**(10), 3365–3387 (2020)
52. Yang, X., Chen, C., Yang, X., Liu, F., Lin, G.: Text-to-image rectified flow as plug-and-play priors. *arXiv preprint arXiv:2406.03293* (2024)
53. Yang, Z., Teng, J., Zheng, W., Ding, M., Huang, S., Xu, J., Yang, Y., Hong, W., Zhang, X., Feng, G., et al.: Cogvideox: Text-to-video diffusion models with an expert transformer. *arXiv preprint arXiv:2408.06072* (2024)
54. Yu, J., Wang, Y., Zhao, C., Ghanem, B., Zhang, J.: Freedom: Training-free energy-guided conditional diffusion model. In: *Proceedings of the IEEE/CVF International Conference on Computer Vision*. pp. 23174–23184 (2023)
55. Zhan, Z., Chen, D., Mei, J.P., Zhao, Z., Chen, J., Chen, C., Lyu, S., Wang, C.: Conditional image synthesis with diffusion models: A survey. *arXiv preprint arXiv:2409.19365* (2024)
56. Zhang, L., Rao, A., Agrawala, M.: Adding conditional control to text-to-image diffusion models. In: *Proceedings of the IEEE/CVF international conference on computer vision*. pp. 3836–3847 (2023)

57. Zhang, R., Isola, P., Efros, A.A., Shechtman, E., Wang, O.: The unreasonable effectiveness of deep features as a perceptual metric. In: Proceedings of the IEEE conference on computer vision and pattern recognition. pp. 586–595 (2018)
58. Zheng, K., He, G., Chen, J., Bao, F., Zhu, J.: Diffusion bridge implicit models. arXiv preprint arXiv:2405.15885 (2024)
59. Zhou, L., Lou, A., Khanna, S., Ermon, S.: Denoising diffusion bridge models. arXiv preprint arXiv:2309.16948 (2023)

# Appendix

This appendix is organized as follows:

- Section A.1 gives the proof of equivalent marginal distributions between the reversed-SDE and its corresponding PF-ODE.
- Section A.2 demonstrates the detailed derivation of  $h_{x_0=\tilde{y}}$ .
- Section A.3 provides the Weighted  $h$ -Transform Inference equation for velocity-based Optimal Transport Flow Matching (OT-FM) and noise-based Variance-Preserving SDE (VP-SDE).
- Section A.4 indicates the implementation details of our method, including how we obtain the coarse videos, text prompts of video generation, and how we set related hyperparameters.
- Section A.5 provides additional results, including the ablation study of weight function  $\lambda$  and additional qualitative results.
- Section A.6 shows the extension of our method on the image editing task.

## A.1 Equivalence Proof of Marginal Distributions

In this section, we provide the formal proof that the stochastic differential equation (SDE) in Eq. (6) and the ordinary differential equation (ODE) in Eq. (7) share the same marginal distribution.

Let  $q_t(\mathbf{x}_t)$  denote the marginal probability density of the latent  $\mathbf{x}_t$  at time  $t$ . We first write the drift term of the SDE (Eq. (6)) as:

$$\boldsymbol{\mu}_{\text{SDE}}(\mathbf{x}_t, t) = \mathbf{f}(\mathbf{x}_t, t) - g^2(t)\nabla_{\mathbf{x}_t} \log p_t(\mathbf{x}_t) - g^2(t)\mathbf{h}_{\mathbf{x}_0=\mathbf{y}} \quad (\text{A16})$$

The evolution of the probability density  $q_t(\mathbf{x}_t)$  for this reverse-time SDE is governed by the Fokker-Planck equation [30] (F-P equation). Taking into account the negative time increment in the reverse process, the corresponding F-P equation is given by:

$$\frac{\partial q_t}{\partial t} = -\nabla \cdot (\boldsymbol{\mu}_{\text{SDE}}q_t) - \frac{1}{2}g^2(t)\Delta q_t \quad (\text{A17})$$

Then, we substitute the mathematical identity  $\Delta q_t = \nabla \cdot (\nabla q_t) = \nabla \cdot (q_t \nabla \log q_t)$  into Eq. (A17) yields:

$$\frac{\partial q_t}{\partial t} = -\nabla \cdot (\boldsymbol{\mu}_{\text{SDE}}q_t) - \frac{1}{2}g^2(t)\nabla \cdot (q_t \nabla \log q_t) \quad (\text{A18})$$

We can reformulate the equation as a standard continuity equation:

$$\frac{\partial q_t}{\partial t} = -\nabla \cdot \left( \underbrace{\left[ \boldsymbol{\mu}_{\text{SDE}} + \frac{1}{2}g^2(t)\nabla \log q_t \right]}_{\mathbf{v}_{\text{ODE}}} q_t \right) \quad (\text{A19})$$

Eq. (A19) takes the form  $\frac{\partial q_t}{\partial t} = -\nabla \cdot (\mathbf{v}_{\text{ODE}}q_t)$ , which precisely describes the density evolution of a deterministic ODE  $d\mathbf{x} = \mathbf{v}_{\text{ODE}}dt$ . Therefore, the equivalent deterministic drift  $\mathbf{v}_{\text{ODE}}$  that shares the same marginal density  $q_t$  is:

$$\mathbf{v}_{\text{ODE}} = \boldsymbol{\mu}_{\text{SDE}} + \frac{1}{2}g^2(t)\nabla \log q_t(\mathbf{x}_t) \quad (\text{A20})$$

In the context of diffusion models, the goal of introducing the additional term  $\mathbf{h}_{\mathbf{x}_0=\mathbf{y}}$  is to shift the unconditional score to the target conditional score. By definition, the exact marginal score of the process is structurally related to the unconditional score via:

$$\nabla \log q_t(\mathbf{x}_t) = \nabla_{\mathbf{x}_t} \log p_t(\mathbf{x}_t) + \mathbf{h}_{\mathbf{x}_0=\mathbf{y}} \quad (\text{A21})$$

Finally, we substitute the definition of  $\boldsymbol{\mu}_{\text{SDE}}$  and the score identity from Eq. (A21) into Eq. (A20):

$$\begin{aligned} \mathbf{v}_{\text{ODE}} &= [\mathbf{f}(\mathbf{x}_t, t) - g^2(t)\nabla_{\mathbf{x}_t} \log p_t(\mathbf{x}_t) - g^2(t)\mathbf{h}_{\mathbf{x}_0=\mathbf{y}}] \\ &\quad + \frac{1}{2}g^2(t)(\nabla_{\mathbf{x}_t} \log p_t(\mathbf{x}_t) + \mathbf{h}_{\mathbf{x}_0=\mathbf{y}}) \end{aligned} \quad (\text{A22})$$

Simplifying the terms, we obtain:

$$\mathbf{v}_{\text{ODE}} = \mathbf{f}(\mathbf{x}_t, t) - \frac{1}{2}g^2(t) (\nabla_{x_t} \log p_t(\mathbf{x}_t) + \mathbf{h}_{\mathbf{x}_0=\mathbf{y}}) \quad (\text{A23})$$

This derived drift  $\mathbf{v}_{\text{ODE}}$  is identical to the drift of the ODE presented in Eq. (7). Since the same continuity equation governs the probability density of the given SDE and this resulting ODE, we conclude that they exhibit the same marginal distribution  $q_t(\mathbf{x}_t)$  at all times  $t$ .

## A.2 Derivation of $\mathbf{h}_{\mathbf{x}_0=\tilde{\mathbf{y}}}$

In this section, we provide the detailed derivation of  $\mathbf{h}_{\mathbf{x}_0=\tilde{\mathbf{y}}}$ .

Based on Eq. (10), we can get the probability density function of  $p_t(\mathbf{x}_t|\mathbf{x}_0 = \tilde{\mathbf{y}})$ :

$$p_t(\mathbf{x}_t|\mathbf{x}_0 = \tilde{\mathbf{y}}) = \frac{1}{(2\pi\sigma_t^2)^{d/2}} \exp\left(-\frac{\|\mathbf{x}_t - \alpha_t\tilde{\mathbf{y}}\|^2}{2\sigma_t^2}\right). \quad (\text{A24})$$

Then take the log of both sides of the equation and calculate the gradient:

$$\begin{aligned} \nabla_{\mathbf{x}_t} \log p_t(\mathbf{x}_t|\mathbf{x}_0 = \tilde{\mathbf{y}}) &= \nabla_{\mathbf{x}_t} \left[ -\frac{d}{2} \log(2\pi\sigma_t^2) - \frac{\|\mathbf{x}_t - \alpha_t\tilde{\mathbf{y}}\|^2}{2\sigma_t^2} \right] \\ &= -\frac{1}{2\sigma_t^2} \nabla_{\mathbf{x}_t} \|\mathbf{x}_t - \alpha_t\tilde{\mathbf{y}}\|^2 \\ &= -\frac{2(\mathbf{x}_t - \alpha_t\tilde{\mathbf{y}})}{2\sigma_t^2} \\ &= -\frac{\mathbf{x}_t - \alpha_t\tilde{\mathbf{y}}}{\sigma_t^2} = \frac{1}{\sigma^2}(\alpha_t\tilde{\mathbf{y}} - \mathbf{x}_t). \end{aligned} \quad (\text{A25})$$

Then we substitute it into Eq. (9) and get the final  $\mathbf{h}_{\mathbf{x}_0=\tilde{\mathbf{y}}}$ , *i.e.*, Eq. (12).

### A.3 Weighted $h$ -Transform Inference for Various SDEs

We derived our method, Weighted  $h$ -Transform Inference from the Score Matching perspective in our paper, and we claim that our method is compatible with other diffusion models like DDPM and Flow Matching. In this section, we provide the derivation of the inference equation of  $v$ -based Optimal Transport Flow Matching (OT-FM) and  $\epsilon$ -based Variance-Preserving SDE (VP-SDE).

**OT-FM with  $v$ -prediction.** In Flow Matching, the velocity field  $v_\theta(\mathbf{x}_t, t)$  corresponds to the PF-ODE drift. Thus, we have the relation:

$$v_\theta = \mathbf{f}(\mathbf{x}_t, t) - \frac{1}{2}g^2(t)s_\theta \implies \frac{1}{2}g^2(t)s_\theta = \mathbf{f}(\mathbf{x}_t, t) - v_\theta \quad (\text{A26})$$

Substituting this relation into the ODE (Eq. (15)), we rewrite the drift in terms of  $v_\theta$ :

$$\begin{aligned} d\mathbf{x} &= \left[ v_\theta + \lambda_\sigma \left( \frac{g^2(t)}{2\sigma_t^2}(\mathbf{x}_t - \alpha_t \tilde{\mathbf{y}}) + \frac{1}{2}g^2(t)s_\theta \right) \right] dt \\ &= \left[ v_\theta + \lambda_\sigma \left( \frac{g^2(t)}{2\sigma_t^2}(\mathbf{x}_t - \alpha_t \tilde{\mathbf{y}}) + \mathbf{f}(\mathbf{x}_t, t) - v_\theta \right) \right] dt \end{aligned} \quad (\text{A27})$$

For OT-FM, the trajectory is defined by  $\sigma_t = 1 - \alpha_t$ . Under a linear schedule where  $\alpha_t = 1 - t$  and  $\sigma_t = t$ , we have  $\dot{\alpha}_t = -1$  and  $\dot{\sigma}_t = 1$ . The corresponding drift and squared diffusion coefficients are:

$$\mathbf{f}(\mathbf{x}_t, t) = \frac{\dot{\alpha}_t}{\alpha_t} \mathbf{x}_t \quad (\text{A28})$$

$$g^2(t) = 2\sigma_t \dot{\sigma}_t - 2 \frac{\dot{\alpha}_t}{\alpha_t} \sigma_t^2 = -2\dot{\alpha}_t \sigma_t \left( 1 + \frac{\sigma_t}{\alpha_t} \right) = -2\dot{\alpha}_t \frac{\sigma_t}{\alpha_t} \quad (\text{A29})$$

We now simplify the guidance term from Eq. (A27) using these coefficients:

$$\begin{aligned} \frac{g^2(t)}{2\sigma_t^2}(\mathbf{x}_t - \alpha_t \tilde{\mathbf{y}}) + \mathbf{f}(\mathbf{x}_t, t) &= \frac{-2\dot{\alpha}_t \frac{\sigma_t}{\alpha_t}}{2\sigma_t^2}(\mathbf{x}_t - \alpha_t \tilde{\mathbf{y}}) + \frac{\dot{\alpha}_t}{\alpha_t} \mathbf{x}_t \\ &= -\frac{\dot{\alpha}_t}{\alpha_t \sigma_t}(\mathbf{x}_t - \alpha_t \tilde{\mathbf{y}}) + \frac{\dot{\alpha}_t}{\alpha_t} \mathbf{x}_t \\ &= \mathbf{x}_t \dot{\alpha}_t \left( \frac{1}{\alpha_t} - \frac{1}{\alpha_t \sigma_t} \right) + \frac{\dot{\alpha}_t}{\sigma_t} \tilde{\mathbf{y}} \end{aligned} \quad (\text{A30})$$

Using the OT constraint  $\sigma_t - 1 = -\alpha_t$ , the term simplifies perfectly:

$$\mathbf{x}_t \dot{\alpha}_t \left( \frac{\sigma_t - 1}{\alpha_t \sigma_t} \right) + \frac{\dot{\alpha}_t}{\sigma_t} \tilde{\mathbf{y}} = -\frac{\dot{\alpha}_t}{\sigma_t} \mathbf{x}_t + \frac{\dot{\alpha}_t}{\sigma_t} \tilde{\mathbf{y}} = -\dot{\alpha}_t \left( \frac{\mathbf{x}_t - \tilde{\mathbf{y}}}{\sigma_t} \right) \quad (\text{A31})$$

Since  $\dot{\alpha}_t = -1$ , this term evaluates exactly to  $\frac{\mathbf{x}_t - \tilde{\mathbf{y}}}{\sigma_t}$ . Substituting this back into Eq. (A27) yields the final velocity-based guided ODE:

$$d\mathbf{x} = \left[ v_\theta + \lambda_\sigma \left( \frac{\mathbf{x}_t - \tilde{\mathbf{y}}}{\sigma_t} - v_\theta \right) \right] dt \quad (\text{A32})$$

**VP-SDE with  $\epsilon$ -Prediction.** For a VP forward process  $\mathbf{x}_t = \alpha_t \mathbf{x}_0 + \sigma_t \epsilon$  constrained by  $\alpha_t^2 + \sigma_t^2 = 1$ , the drift and diffusion coefficients are also uniquely determined by the schedule  $\alpha_t$ , *i.e.*, Eq. (A28) and Eq. (A29).

In the  $\epsilon$ -prediction framework, the score function is parameterized as  $s_\theta = -\frac{\epsilon_\theta}{\sigma_t}$ . Substituting  $\mathbf{f}$ ,  $g^2(t)$ , and  $s_\theta$  into Eq. (15), we obtain:

$$\begin{aligned} d\mathbf{x} &= \left[ \frac{\dot{\alpha}_t}{\alpha_t} \mathbf{x}_t - \frac{1}{2} \left( -2 \frac{\dot{\alpha}_t}{\alpha_t} \right) \left( -\frac{\epsilon_\theta}{\sigma_t} + \lambda_\sigma \left( \frac{\alpha_t \tilde{\mathbf{y}} - \mathbf{x}_t}{\sigma_t^2} + \frac{\epsilon_\theta}{\sigma_t} \right) \right) \right] dt \\ &= \frac{\dot{\alpha}_t}{\alpha_t} \left[ \mathbf{x}_t - \frac{1}{\sigma_t} \left( \epsilon_\theta - \lambda_\sigma \left( \frac{\alpha_t \tilde{\mathbf{y}} - \mathbf{x}_t}{\sigma_t} + \epsilon_\theta \right) \right) \right] dt \end{aligned} \quad (\text{A33})$$

We define the pseudo-target noise corresponding to the condition  $\tilde{\mathbf{y}}$  as:

$$\tilde{\epsilon} = \frac{\mathbf{x}_t - \alpha_t \tilde{\mathbf{y}}}{\sigma_t} \quad (\text{A34})$$

By observing that  $\frac{\alpha_t \tilde{\mathbf{y}} - \mathbf{x}_t}{\sigma_t} = -\tilde{\epsilon}$ , we can substitute this into the inner guidance term in Eq. (A33):

$$\epsilon_\theta - \lambda_\sigma (-\tilde{\epsilon} + \epsilon_\theta) = \epsilon_\theta + \lambda_\sigma (\tilde{\epsilon} - \epsilon_\theta) \quad (\text{A35})$$

This reveals the effective guided noise prediction  $\hat{\epsilon}_\theta$ :

$$\hat{\epsilon}_\theta = \epsilon_\theta + \lambda_\sigma (\tilde{\epsilon} - \epsilon_\theta) \quad (\text{A36})$$

Consequently, the guided PF-ODE simplifies elegantly to the standard unguided formulation, driven entirely by the linearly interpolated noise  $\hat{\epsilon}_\theta$ :

$$d\mathbf{x} = \frac{\dot{\alpha}_t}{\alpha_t} \left( \mathbf{x}_t - \frac{\hat{\epsilon}_\theta}{\sigma_t} \right) dt \quad (\text{A37})$$

## A.4 Implementation details

**Obtaining the Coarse Videos.** In Section 5.2, we use 3-D models to render an image into a corresponding coarse warped video based on its camera intrinsics and poses. First, we leverage a pretrained depth estimation model, DepthPro [2], to get the depth map of the first frame image. Then we reproject this depth map into a point cloud and render a sequence of images for given camera motion poses. To ensure motion quality, we filter out static or minimal-movement sequences where the camera translation extent is less than 8.

To resolve the scale ambiguity of monocular depth maps, we align them with the camera trajectories using SIFT feature matching [29] between the reference frame and subsequent frames (sampled at 5-frame intervals). Matches are refined using a  $k$ -nearest neighbor search ( $k = 2$ ) and a Lowe’s ratio test threshold of 0.75. After computing candidate scales via projection constraints, we discard the top and bottom 5% outliers and apply the median value as the final scale. The reference image is warped to target views by unprojecting valid pixels (depth  $> 0$ ) into 3-D space using the inverse intrinsic matrix and the calibrated depth. These points are transformed into the target camera coordinate system and splatted onto the 2-D image plane.

To correctly resolve self-occlusions during rendering, we implement a  $Z$ -buffering approach by sorting the projected points in descending order of depth. To address deocclusion holes inherently caused by forward splatting, we implement a global nearest-neighbor filling strategy utilizing a  $k$ -d tree built on valid pixel coordinates. The corresponding visibility masks are further refined using morphological opening with a  $5 * 5$  rectangular kernel to eliminate isolated projection noise and smooth edges. More details can be found in the code.

**Image-to-Video Prompts Preparation.** For prompts generation, we follow the protocol of CogVideoX [53], *i.e.*, leverage the pretrained Vision-Language model GPT-4o [16] to generate caption for the given first frame. These generated prompts will be used as the text condition for subsequent image-to-video generation.

**The Implementation of Using Wan2.2 for Camera-controlled Video Generation.** For Wan2.2 [49], we change the length and resolution of evaluated videos, *i.e.*, frame number from 49 into 81 and the resolution from  $720 * 480$  into  $832 * 480$ . During sampling, we set the weight function  $\lambda_\sigma = \sigma^\alpha$  and give these two parts different  $\alpha$ . For the valid part,  $\alpha = 16$  and for the invalid part,  $\alpha = 20$ . For other hyperparameters of Wan2.2, we follow the implementations of TTM [41].

**Table A3:** Ablation study of the weight function  $\lambda$ .

$\lambda$	Super-resolution		Inpainting	
	FID $_{\downarrow}$	LPIPS $_{\downarrow}$	FID $_{\downarrow}$	LPIPS $_{\downarrow}$
$(\frac{t}{T})^3$	40.42	0.380	49.87	0.369
$(\frac{t}{T})^5$	40.80	0.466	51.79	0.461
$(\frac{t}{T})^7$	39.58	0.503	52.80	0.500
$\sigma^3$	35.02	0.208	81.15	0.433
$\sigma^5$	33.61	0.209	35.06	0.117
$\sigma^7$	32.98	0.219	47.99	0.331

## A.5 Additional Results

**Ablation of the Weight Function.** To further explore the influence of the weight function, we ablated it on image super-resolution and inpainting tasks (*cf.*, Section 5.1). As shown in Table A3, we experimented the  $\lambda = (\frac{t}{T})^\alpha$  and  $\lambda = \sigma_t^\alpha$  and gave  $\alpha$  different values. We can observe that when the weight function  $\lambda$  is a  $\sigma_t$ -related function (last three rows), our method can achieve a generally better performance across tasks and metrics. This indicates that our weight function design, which is inspired by the analysis of approximation error (negatively correlated to the noise level  $\sigma_t$ ), is reasonable and effective.

**Additional Qualitative Results.** We provide additional qualitative comparisons with SDEdit [31] (*cf.*, Section 5.1) on four image restoration tasks in Figure A9. Besides, we provide additional qualitative comparisons with TTM [41] and GWTF [3] (*cf.*, Section 5.2) on camera-controlled video generation tasks in Figure A10. Moreover, we gave more camera-controlled video generation results with Wan2.2 as the base model in Figure A11.

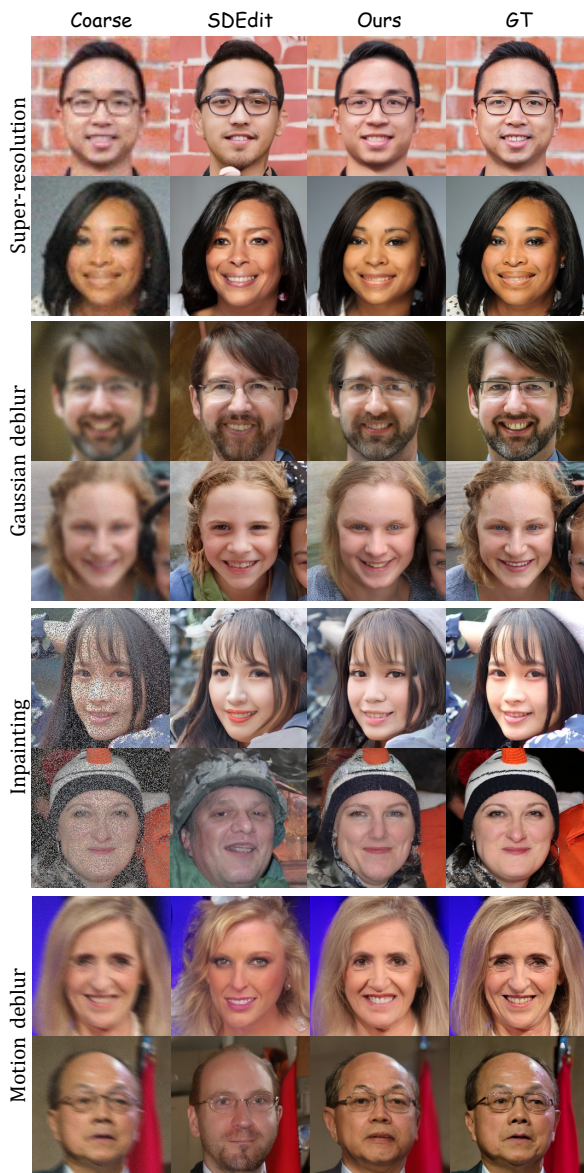


Fig. A9: Additional qualitative comparisons with SDEdit on image restoration tasks.

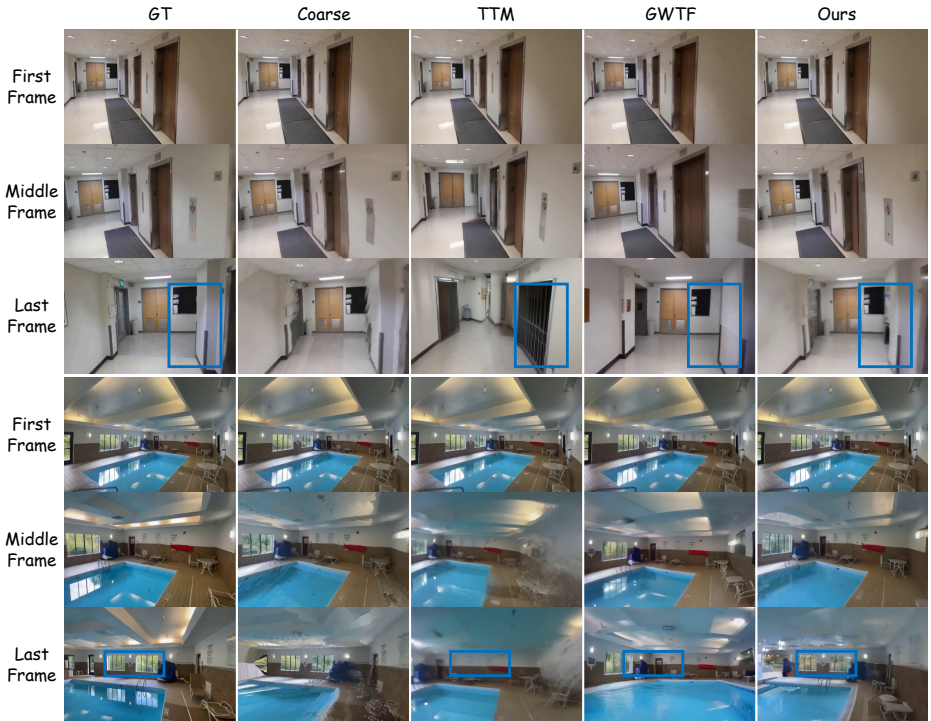


Fig. A10: Additional camera-controlled video generation qualitative comparisons.

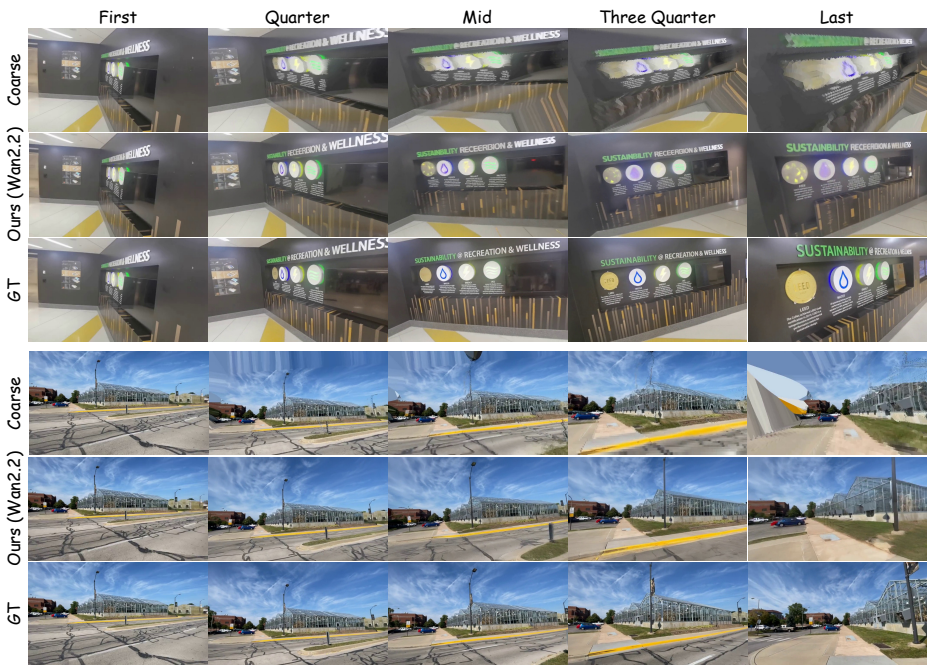


Fig. A11: Additional camera-controlled video generation results using Wan2.2.

**Table A4:** Quantitative comparisons with five baselines for image editing on PIEBench. **Bold:** best, underline: second best.

Method	Source Consistency					Semantic Alignment		
	Distance $\downarrow$	PSNR $\uparrow$	LPIPS $\downarrow$	MSE $\downarrow$	SSIM $\uparrow$	CLIP Entire $\uparrow$	CLIP Edited $\uparrow$	
ODE-Inv	0.074	17.57	0.240	0.024	0.691	24.57	21.73	
SDEdit [31]	0.036	22.57	0.119	0.008	0.747	24.56	21.95	
iRFDS [52]	0.069	18.81	0.191	0.021	0.738	25.12	21.95	
FlowEdit [22]	0.036	23.02	<u>0.082</u>	0.007	<u>0.842</u>	<b>25.98</b>	<b>22.81</b>	
FlowAlign [20]	<u>0.028</u>	<u>25.50</u>	<b>0.053</b>	<b>0.004</b>	<b>0.879</b>	25.28	22.00	
Ours	<b>0.017</b>	<b>25.98</b>	0.097	<b>0.004</b>	0.819	<u>25.41</u>	<u>22.37</u>	

## A.6 Image Editing

To further explore the generalization ability of our method, we conducted the experiments on a text-based image editing task, *i.e.*, given a source image, a source prompt, and a target prompt, we want to edit the source image into a target image according to the description of the target prompt. Specifically, our method use the source image as the  $\tilde{\mathbf{y}}$  and the  $s_\theta$  is the predicted score by a pretrained text-to-image models that adopt the target prompt as the condition. We set the sampling timestep as 50, and the target guidance scale was set to 13.5, and the weight function is  $\lambda_\sigma = \sigma_t$ .

We compared our method with five state-of-the-art flow-based editing methods that were implemented with SD-3-medium [11]: 1) *ODE inversion (ODE-Inv)*, which gets the inversion by using the Euler Solver and denoises with the target prompt. 2) *SDEdit* [31], which adds random noise and then denoises with the target prompt. 3) *iRFDS* [52], which is a SDS-based editing method. 4) *FlowEdit* [22] and 5) *FlowAlign* [20] are two inversion-free editing methods. The results of these baselines are from *FlowAlign* [20]. We evaluated on PIEBench [17] and reported the seven commonly used metrics to evaluate both source consistency (*Structure Distance*, *Background PSNR*, *Background LPIPS*, *Background MSE*, *Background SSIM*) and Semantic Alignment (*Entire CLIP Score* and *Edited CLIP Score*).

As shown in Table A4, our method can outperform the *ODE-Inv*, *SDEdit* and *iRFDS*. Meanwhile, we can perform competitively against their current strong methods, *e.g.*, *FlowEdit* and *FlowAlign*. As a highlight, our method achieves such a performance even without incorporating the source prompt as the prior. We also gave qualitative comparisons in Figure A12. We can see that our results show a superior editing performance (better balance between the source consistency and target semantic alignment) than baselines.

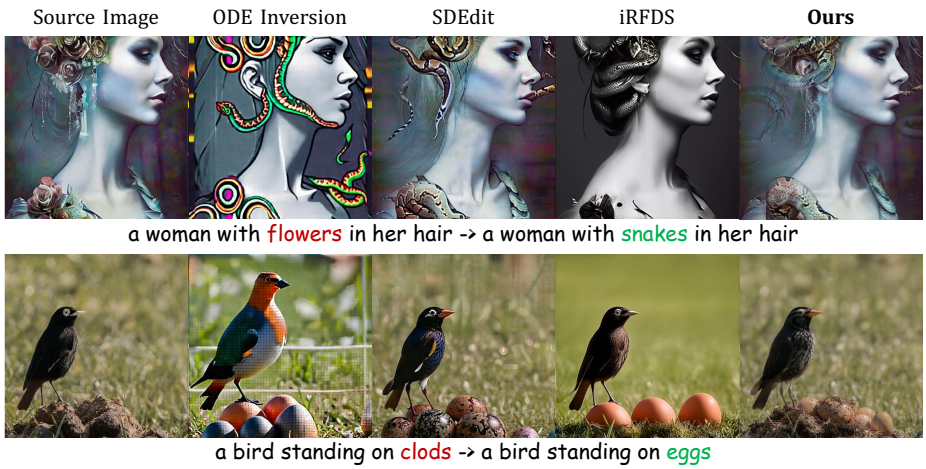


**Fig. A12:** Text-based image editing comparisons with three baselines on PIE-Bench